Electronic Supporting Information (ESI)

The two step LASiS-GRR method involves using two metal targets (Co and Cu) for ablation in K_2PtCl_4 solution alternately. The EDX mapping results in Fig. S1 reveal the formation of PtCuCo ternary NAs, however, the elemental distribution is relatively less uniform in comparison with the one-step LASiS-GRR NAs shown in the main article. This is because the first metal (Cu) seeding NPs might have already developed into different oxidation or nucleation states during LASiS-GRR on the second metal (Co), thereby rendering the latter alloying process to be non-uniform. To confirm the first metal NPs have not got fully oxidized in water and can still be active for GRR at the second-step, another sample was prepared by first laser ablating Co in water for 5 min, then instantly mixing the colloidal solution with K_2PtCl_4 and stirring it overnight, where GRR was carried out without use of a laser. Although PtCo nanoalloys are formed, as confirmed by the EDX mapping and SAED pattern in Fig. S2, nonetheless, the XRD profile indicates the productivity is almost negligible. This suggests a large portion of seeding Co have already gone through the initial nucleation and crystal growth, however, a small portion of Co can still sustain at a lower oxidation state for a certain period of time before being fully oxidized. Besides, laser ablation/radiation plays a critical role in enabling GRR to occur extensively.

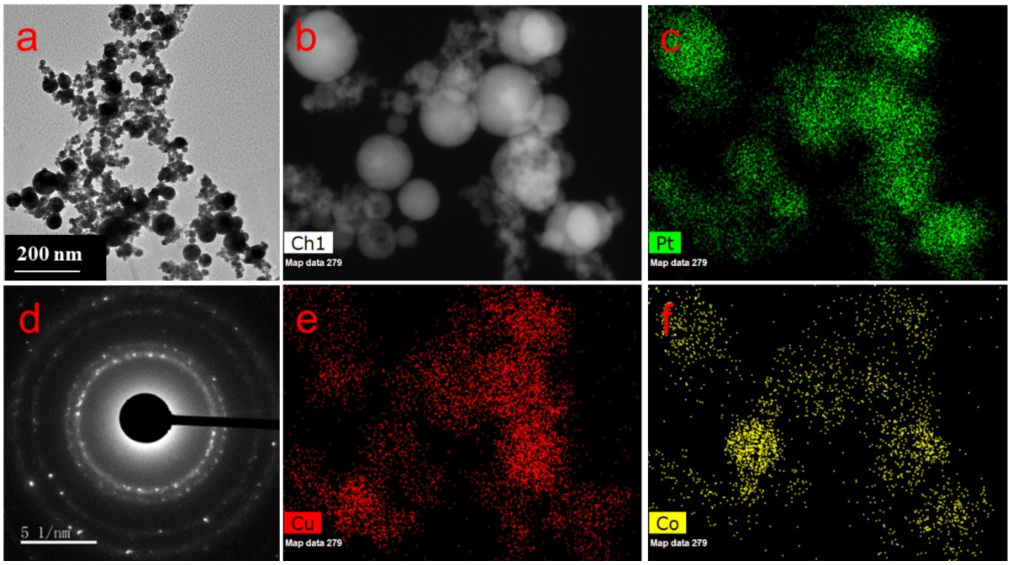

Fig. S1 TEM and EDX characterizations for PtCuCo ternary NAs synthesized via the two-step LASiS-GRR method. **a.** TEM image; **d.** the corresponding SAED pattern; **b.** High angle annular dark field (HAADF) scanning TEM image; **c, e, f.** the corresponding Pt, Cu and Co mappings for **b**.

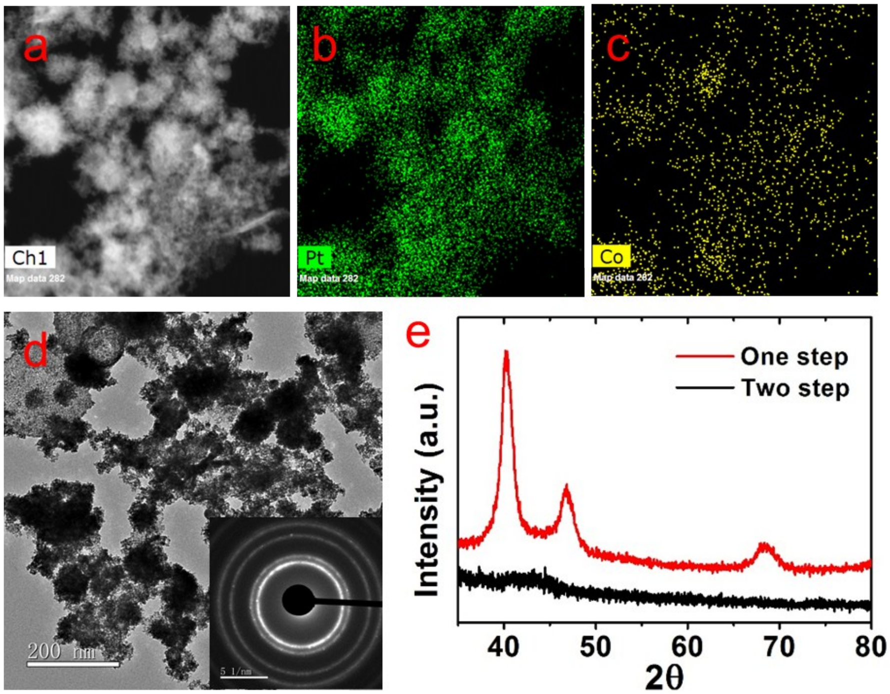

Fig. S2 EDX mappings (**a-c**) and TEM image (**d**) of the two step method synthesized PtCo NAs, with the inset in **d** shows the SAED pattern; **e.** XRD comparison of the PtCo NAs synthesized via LASiS-GRR (one step) and the two step method.

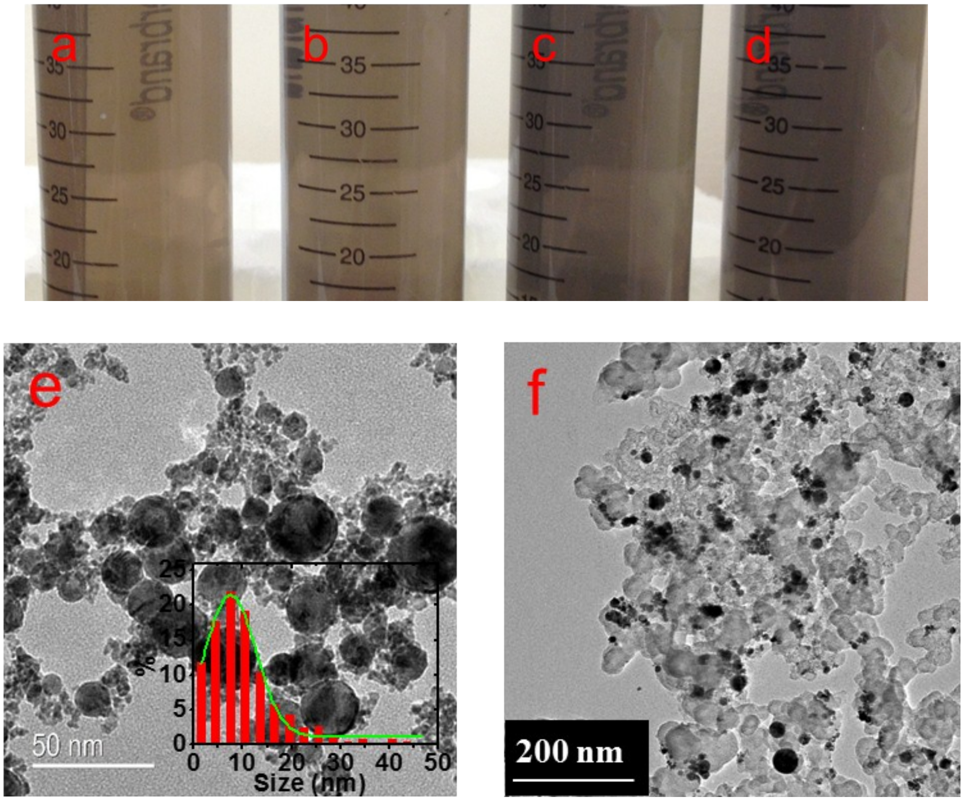

Fig. S3 PtCuCo colloidal solutions right after LASiS-GRR (pH7). From **a** to **d**, PtCo-1, PtCuCo-1, PtCuCo-2, PtCuCo-3 respectively; **e.** enlarged TEM image of PtCuCO-2 along with the particle size distribution showing in inset; **f.** TEM image of PtCuCo NAs embedded in carbon black (Vulcan XC 72R).

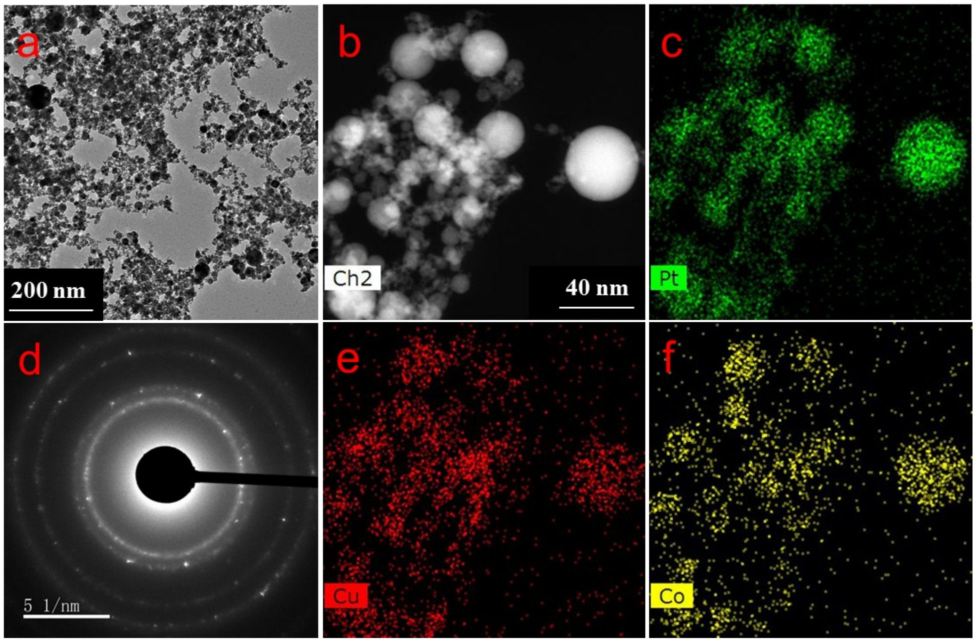

Fig. S4 TEM and EDX characterizations for PtCuCo-4 (pH11). **a.** TEM image; **d.** the corresponding SAED pattern; **b.** High angle annular dark field (HAADF) scanning TEM image; **c, e, f.** the corresponding Pt, Cu and Co mappings for **b**.

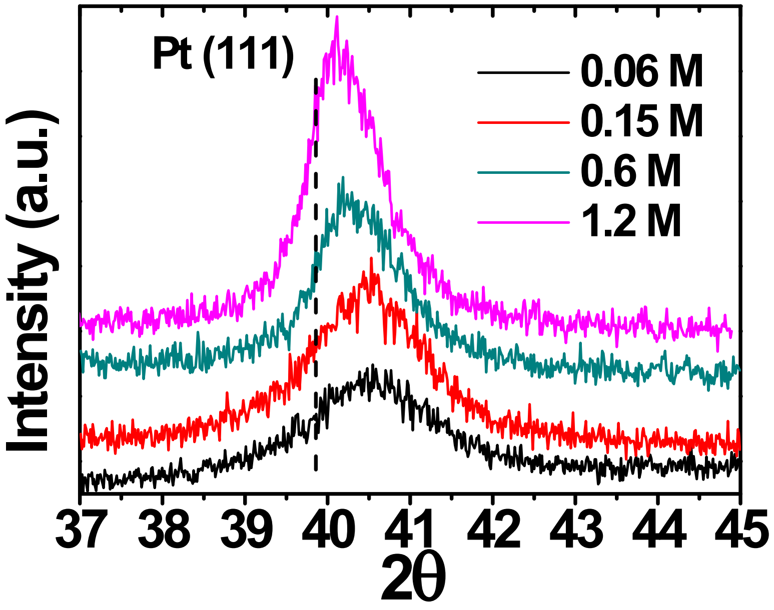

Fig. S5 XRD patterns for the PtCuCo ternary NA samples synthesized using different initial [K_2PtCl_4] in this study. The dash lines mark the standard peak position for Pt (111).

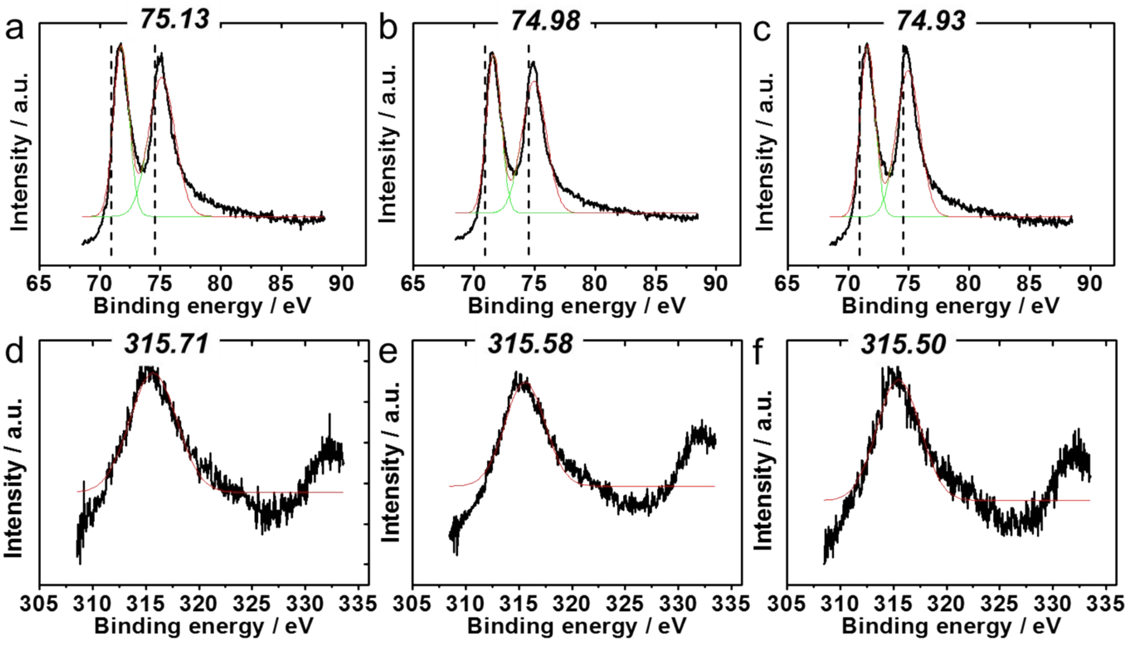

Fig. S6 Pt 4f $_{7/2}$ (**a-c**) and Pt 4d $_{5/2}$ (**d-f**) peaks in XPS spectra. **a, d.** PtCo-1; **b, e.** PtCuCo-2; **c, f.** PtCuCo-4. The value on each image tells the corresponding peak position from the fitting.

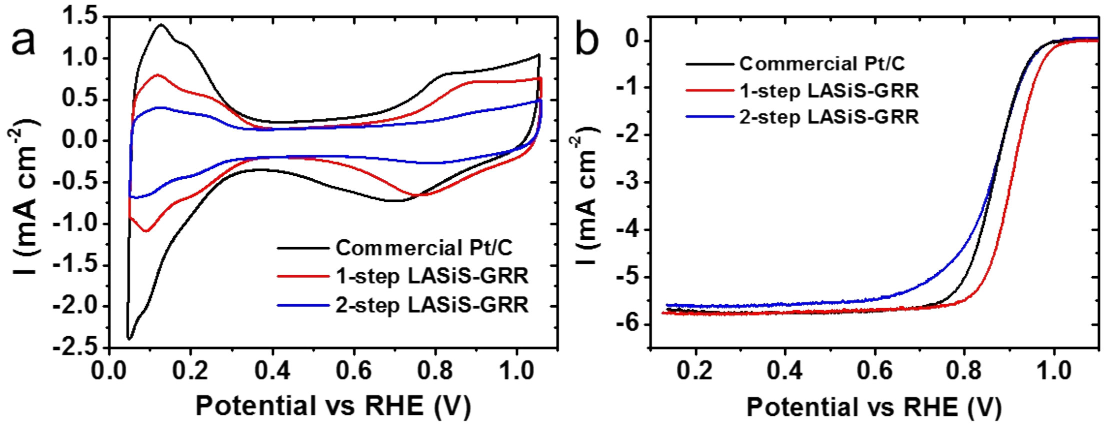

Fig. S7 Electrochemistry data indicating ORR activities of the PtCuCo ternary NAs made via the two LASiS-GRR methods when compared to commercial Pt/C samples using **a.** Cyclic voltammetry curves at a scan rate of 100 mV/s; **b.** ORR polarization curves at 1600 rpm and scan rate of 5 mV/s.

The dynamics of the electron transfer process in ORR were analyzed through the rotating disk voltammetry (RDV) at different speeds (ranging between 400-2200 rpm) based on the Koutecky-Levich (KL) equation:

$$\frac{1}{J}=\frac{1}{J_K}+\frac{1}{J_L}=\frac{1}{J_K}+\frac{1}{B\omega^{1/2}}$$

$$J_K = nFkC_0\,;\ B = 0.62nFC_0D_0^{2/3}\nu^{-1/6}$$

where J, J_K and J_L are the measured, kinetic and diffusion limiting current densities respectively, n is the electron transfer number, F is the Faraday constant (96 485 C mol^{-1}), C_o and D_o are the dissolved O_2 concentration the O_2 diffusion coefficient in the electrolyte respectively, v is the electrode rotation rate in rpm. Tafel plots are generated using the kinetic current J_K as determined from:

$$J_K=\frac{J*J_L}{J_L-J}$$

The electrochemical surface area (ECSA) was determined by the hydrogen desorption area in the CV curve between 0.05 to 0.4 V vs. RHE based on the following equation:

$$ECSA=\frac{Q_H}{m\times q_H}$$

where Q_H is the charge for hydrogen desorption, m is the loading amount of metal in the electrode, and q_H is the charge required for monolayer desorption of hydrogen on Pt (210 μC/cm^2).

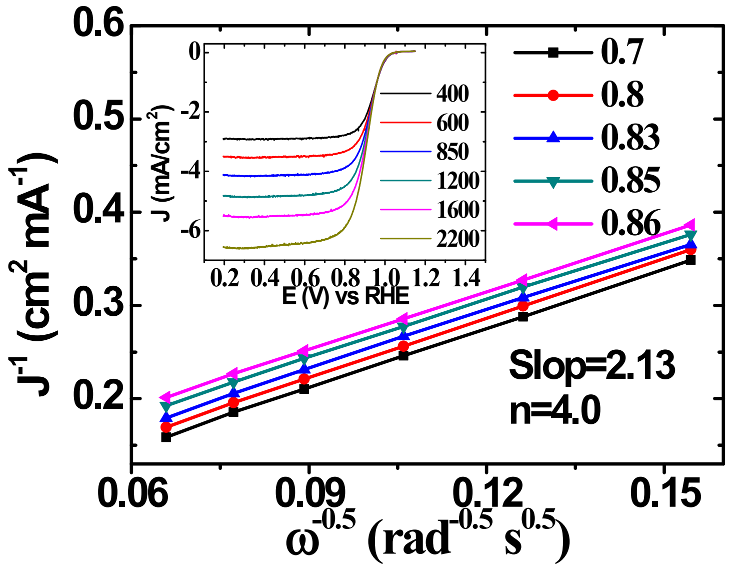

Fig. S8 Koutecky-Levich plots from rotating disk voltammogram (RDV) data (shown in inset) for PtCuCo-2 at different potentials indicating four electron transport process for ORR.

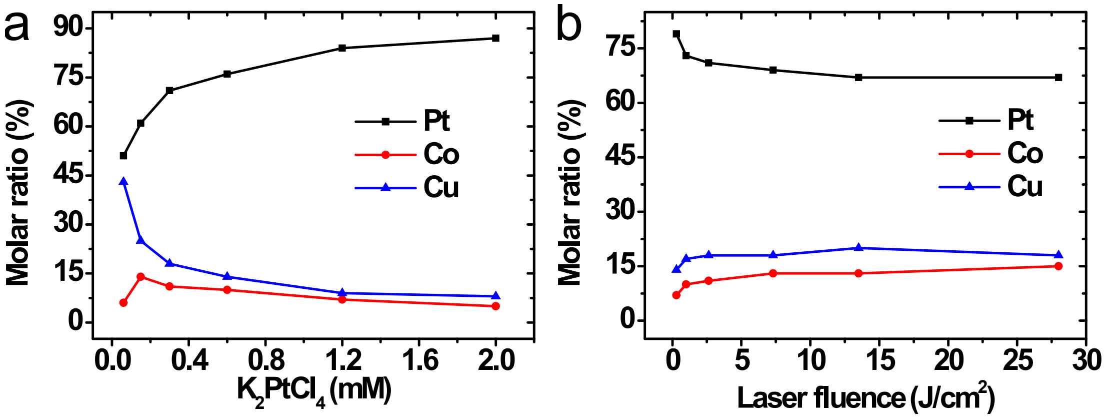

Fig. S9 ICP-OES measurements to study the variations of the elemental ratios (Molar ratio, % for Pt, Co and Cu) in PtCuCo ternary NAs synthesized via LASiS-GRR. **a.** with different initial [K_2PtCl_4] (initial [CuCl] = 0.48 mM, ablating time = 6 min); **b.** at different laser fluence (initial [K_2PtCl_4] = 0.3 mM, [CuCl] = 0.48 mM, ablating time = 6 min).

The synthetic details for the three types of Pt-based ternary NA combinations that exhibit the best ORR activity in each case are summarized in Table S2. Two critical factors need to be taken into consideration for choosing a proper elemental combination, namely, matching of redox potential gradient as well as the target metal/metal oxides solubility in the acid used in the wash step. As mentioned in the introduction, GRR occurs when the target metal carries a relatively lower redox potential than the metal precursor salt. In the case of two metal precursor salts, the redox potential gradients among the three elements will also largely impact the resultant elemental ratio in the alloy. Table S3 summarizes the redox potential values for a few transition metals, from which we rationally designed three ternary metal combinations including PtRu(Ni), PtCo(Mn) and PtNi(Ti). The brackets here indicate the target metals being ablated, which carry certain redox gap to the correspondent two precursor salts for all the samples. Once the initial LASiS-GRR has been carried out, the subsequent washing step determines whether or how well can the superfluous target metal oxides be washed away and in turn brings about the Pt-rich shell-core fine structure. HCl is a well-known acid used in the wash cycle due to its high volatility. As is shown in Table S4, cobalt oxides (CoO/Co_3O_4) exhibit highest solubility in HCl, followed by CuO/Cu_2O, MnO, NiO, while TiO_2 is almost insoluble.

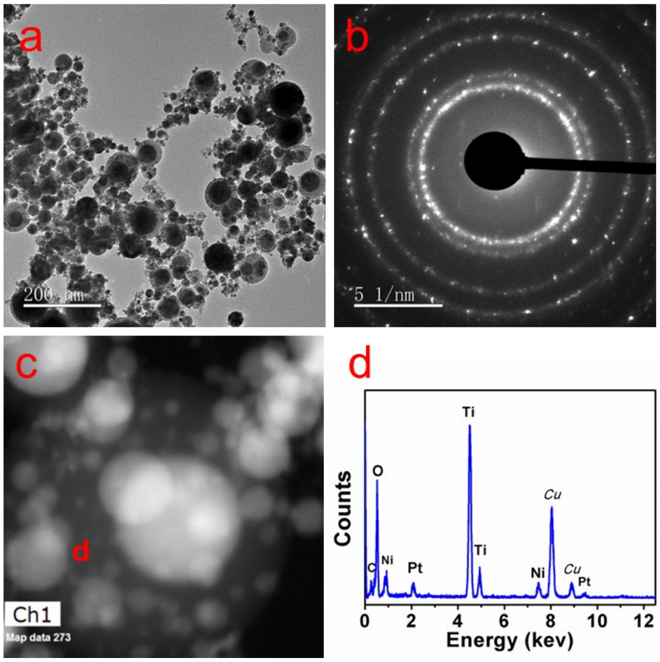

Fig. S10 TEM (**a**), SAED (**b**) and high resolution HAADF image (**c**) for PtNiTi ternary NAs synthesized via LASiS-GRR. **d.** EDX spectra of the corresponding position in **c**. (The Cu signal in **d** corresponds to the Cu grid).

Table S1 Detailed XRD results ((111) peak) for the PtCo and PtCuCo ternary NAs.

NAs	2θ	d / Å	FWHM	Mean size / nm
PtCo	40.20	2.2412	1.37	6.17
PtCuCo-1	40.19	2.2420	1.4	6.04
PtCuCo-2	40.34	2.2338	1.39	6.09
PtCuCo-3	40.24	2.2392	1.34	6.31
PtCuCo-4	40.51	2.2250	1.46	5.80

Table S2 Summary of elemental ratio and mean crystal size of the PtCuCo ternary NAs synthesized with different K_2PtCl_4 concentrations and laser fluences. UF and F represents using unfocused and focused lasers respectively.

K_2PtCl_4 (mM)	CuCl (mM)	Ablation time (min)	Laser fluence (J/cm^2)	Pt%	Co%	Cu%	Mean size / nm
0.06	0.48	6	2.63 (UF)	51	6	43	4.36
0.15				61	14	25	5.39
0.3				71	11	18	6.31
0.6				76	10	14	7.42
1.2				84	7	9	8.90
2				87	5	8	8.96
0.3			0.3 (UF)	79	7	14	5.03
			1 (UF)	73	10	17	5.22
			2.63 (UF)	71	11	18	6.31
			7.3 (F)	69	13	18	6.21
			13.5 (F)	67	13	20	6.45
			28 (F)	67	15	18	6.94

Table S3 Detailed experimental parameters for preparation of various ternary NAs in study.

NAs	Target	Second precusor salt (beside K_2PtCl_4)	Concentration (mM)	Ablation time (min)	Washing Condition
PtCuCo	Co	CuCl	0.16	6	HCl (0.01 M)
PtCoMn	Mn	$CoCl_2$	2.4	3	HCl (0.05 M)
PtRuNi	Ni	$RuCl_2 \cdot 6H_2O$	0.32	5	HCl (0.2 M)
PtNiTi	Ti	$NiCl_2$	1.2	10	HCl (1 M)

Table S4 Redox potential chart for metals in this study.

Redox Couple	**NHE / mV**
$[PtCl_4]^{2-}/Pt$	0.76
Cu^+/Cu	0.52
Ru^{2+}/Ru	0.46
Ni^{2+}/Ni	-0.26
Co^{2+}/Co	-0.28
Mn^{2+}/Mn	-1.18
Ti^{2+}/Ti	-1.63

Table S5 Solubility table for the metal oxides used in this study in different solvents.

Oxides	**Solubility (ppm)**			
	malonic acid	**urea**	**ethylene glycol**	**hydrochloric acid**
CoO	3626	13.6	16	166260
Co_3O_4	5992	30	18.6	142865
Cu_2O	18337	219	394	53942
CuO	14008	4.8	4.6	52047
MnO	6816	0	12	28124
NiO	151	5	9	6109
TiO_2	4	0.5	0.8	36